Original Article

Probing into the properties of B$_4$C reinforced nickel phosphorus-based nanocomposite coating

Osama Fayyaz [a], Moinuddin M. Yusuf [a], Sara Bagherifard [b], M.F. Montemor [c], R.A. Shakoor [a,]*

[a] *Center for Advanced Materials (CAM), Qatar University, 2713, Doha, Qatar*
[b] *Department of Mechanical Engineering, Politecnico di Milano, Milano, Italy*
[c] *Centro de Química Estrutural, Institute of Molecular Sciences, Departamento de Engenharia Química, Instituto Superior Técnico, Universidade de Lisboa, Lisboa 1049-001, Portugal*

ARTICLE INFO

ABSTRACT

Nickel-based coatings are well known for their good corrosion resistance performance. However, these materials suffer from inferior mechanical properties that limit their wider application. This work investigates the synthesis, and performs an exhaustive character-ization, of Ni—P—B$_4$C nanocomposite coatings developed through conventional electrode-position using a modified Watts bath. The study examines the effect of an increase in the concentration of boron carbide nanoparticles (BCNPs) on the structural, morphological, topographical, mechanical and electrochemical properties of the nanocomposite coating. Vickers microhardness tester and nanoindentation technique were utilized to elucidate the role of BCNPs in modifying the mechanical response of nanocomposite coatings. Furthermore, corrosion resistance of the nanocomposite coatings was investigated through d.c potentiodynamic polarization and electrochemical impedance spectroscopy (EIS). Comparison of the properties of the developed coatings revealed the remarkable improvement in the properties of Ni—P—B$_4$C nanocomposite coatings when compared to the bare mild steel substrate and the Ni—P coatings. The enhanced corrosion resistance and superior mechanical properties of Ni—P—B$_4$C nanocomposite coatings make them attractive for many industries. Based upon the experimental findings, a possible mecha-nism for the synthesis and improved corrosion resistance of Ni—P—B$_4$C nanocomposite coatings was also proposed.

1. Introduction

Corrosion is one of the main causes of material failure in various industries. Corrosion damage is typically accelerated in the presence of other failure causes like wear, erosion, fa-tigue and creep. These combined effects are directly or indi-rectly linked to serious damages in various applications such as automobile, water treatment, marine, aerospace, aero-nautical, oil & gas, biomedical and powerplants, piping etc.

[1—3]. NACE reports estimate the global cost of corrosion to be more than $2.5 (US) trillion annually burdening the economic growth of nations around the world [4]. Corrosion also increases the operational cost by unexpected maintenance causing delay and inefficient process flow.

Nickel based metallic coatings are considered as a solution to mitigate corrosion damage in many applications [5,6] and various Nickel-based binary alloy coatings like Ni—B, Ni—W, Ni—P, Ni—Cr and Ni—Cu have been studied. Ni—P coatings are proven to be corrosion resistant; however, to further enhance their mechanical strength they should be reinforced by micron/nanosized hard particles. The resulting properties of the modified composite coatings has attracted attention leading to the production of different materials [5] like Ni—P—TiN [7], Ni—P—Y$_2$O$_3$ [8], Ni—B—Al$_2$O$_3$ [9], Ni—P—ZrO$_2$ [10], Ni—W—SiC [11], Ni—P—Si$_3$N$_4$ [12], Ni—B-YSZ [13], Ni—Cu—TiN [14]. The synthesis of composite coatings can be carried out through different techniques such as electroless deposition, laser cladding, conventional electrodeposition, pulse and reverse pulse deposition methods. Conventional electrodeposition has advantages like bath stability, simple methodology, time efficiency and industrial upgradability over its counterparts making it an attractive process for extensive investigations [5,15].

Boron carbide is a hard and chemically inert ceramic material with a wide range of applications in various industries. Its effectiveness has been exhaustively investigated recently for various applications [16—18]. Jiang et al. [19] fabricated Ni—B4C composite coatings and remarked their superior mechanical strength and corrosion resistance. Rezagholizadeh et al. [20] also reported similar results for Ni—B—B4C nanocomposite coating synthesized through electroless deposition. Hosseinabadi et al. [21], Araghi and Paydar [22], and Monir Vaghefi et al. [23] deposited micron-sized B$_4$C in Ni—P and showed an improvement in tribological properties along with other similar finding in the literature. Teng and coworkers [24] developed Ni—W—B4C nanocomposite coatings and claimed an improvement in micro-hardness and anti-corrosive properties. Although, Bozzini and team worked on the electrodeposition of Ni—P—B4C [25] utilizing sub-micron particles and studied its effect on crystallinity and corrosion—erosion properties of composite coating, there are still important data required to better validate these materials.

This work mainly focusses on the effect of the presence of B4C nanoparticles in Ni—P binary alloy matrix produced from a modified Watt's bath through conventional electrodeposition. Moreover, the effect on the concentration of B$_4$C NP is thoroughly investigated. X-ray diffraction and (XRD) Xray photoelectron spectroscopy (XPS) were utilized to confirm the successful deposition of B4C along with structural properties of nanocomposite coating. Scanning electron Microscopy and Atomic force microscopy were used to study the surface morphology and topography along with microstructural analysis of as prepared coatings. Vickers microhardness and nano indentation were adopted to assess the mechanical properties of nanocomposite coating. Electrochemical measurements were carried out to study the corrosion resistance of coating.

2. Material & characterization

2.1. Materials

Conventional Watts bath was modified for electrodeposition and it was composed of nickel chloride, nickel sulphate, boric acid, sodium chloride, sodium hypophosphite and phosphoric acid in the distilled water as per the description in Table 1. Boron carbide (B$_4$C) nano powder with an average size of 45—55 nm with the purity of 99.9% was purchased from Sigma Aldrich.

2.2. Sample preparation

Ni—P-BCNPs nanocomposite coatings were deposited on polished mild steel substrates. In the first step, the A36 steel sheet was cut into a size of 32-mm coupons. Coupons were ground to produce polished samples on silicon carbide abrasive papers grading from 120, 220, 320, 500, 800, 1000 and 1200. Before getting to the next paper, the samples were washed with soap and water. Sonication was carried after polishing for twenty-five minutes to remove any particles from the polished mild steel substrate. In order to prevent electrodeposition on both sides of the substrates, a protective tape was used to cover the unpolished sides. The steel substrate specimens were etched in a 15% HCl solution for 40 s as a procedure of pre-treatment for removing any of the oxide layer and contaminant over the surface of substrate ensuring adherent and long lasting coating. The substrates were then rinsed in warm distilled water before placing them in the coating chemical bath. The schematic diagram of the electrodeposition experimental system is represented in Fig. 1.

During the electrodeposition process, the nickel sheet served as anode and the polished steel substrate as cathode; these were placed parallel to each other at a distance of ~ 30 mm in the chemical bath. The electrodeposition of Ni—P and Ni—P B$_4$C (0.5 and 1.0 g/L) nanocomposite coating was carried out at 65 °C ± 2. The deposition time was fixed to be 30 min from the initiation of power supply. To avoid settling down of

Table 1 — Chemical bath constituents and operating parameters for co-electrodeposition of Ni—P and Ni—P—B$_4$C nanocomposite coatings.

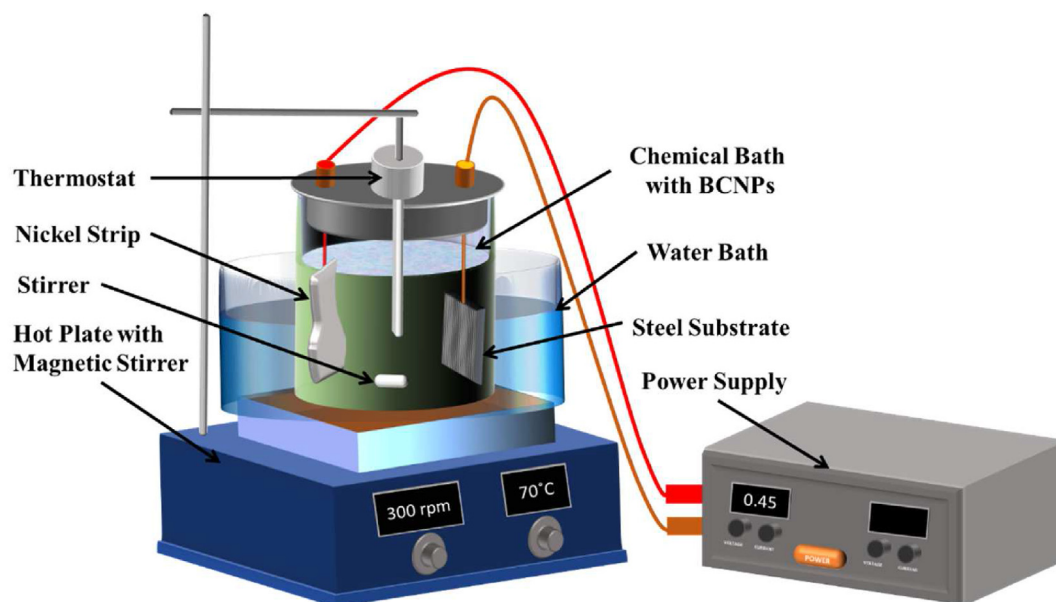| Chemicals	Bath (Ni—P/B$_4$C)
Nickel Sulfate hexahydrate	250 g L^{-1}
Nickel Chloride hexahydrate	15 g L^{-1}
Boric acid	30 g L^{-1}
Sodium Chloride	15 g L^{-1}
Phosphoric acid	6 g L^{-1}
Sodium Hypophosphite	20 g L^{-1}
Boron carbide nanoparticles (B$_4$C < 50 nm)	0, 0.5 and 1.0 g L^{-1}
pH	2.0 ± 0.2
Temperature	65 ± 2 °C
Deposition time	30 min
Current density	48 mA cm^{-2}
Bath agitation	300 rpm

Fig. 1 — Schematic diagram of Ni—P and Ni—P—B₄C electrodeposition process.

the BCNPs, the chemical bath was stirred at 300 ± 5 rpm an hour before initiating electrodeposition. The optimized bath conditions and working parameters are listed Table 1.

2.3. Sample characterization

Structural characterization of the sample was done utilizing X-ray diffractometer (Rigaku. Miniflex2 Desktop, Tokyo, Japan) fitted with Cu Kα radiations with the scanning step of 0.02° in the range of 2θ from 10° to 90°. The morphology of the coatings was studied using a field-emission scanning electron microscope (FE-SEM-Nova Nano-450, Netherlands). Topographical studies were carried out through atomic force microscopy (AFM-USA) device MFP-3D Asylum research (USA) equipped with silicon probe (Al reflex coated Veeco model-OLTESPA, Olympus, spring constant: 2 Nm^{-1}, and resonant frequency: 70 kHz). Measurements were performed under ambient conditions using Standard Topography AC air (tapping mode in the air). Mechanical properties of the samples were tested on Vickers Microhardness tester (FM-ARS9000, USA) and MFP-3D Nanoindenter connected to AFM. The measurement of the microhardness was conducted at 25 gf with a dwell of 10 s. The nanoindentation was evaluated using Berkovich diamond indenter tip with maximum 1 mN indentation force (loading and unloading rate: 200 μN/s and dwell time at maximum load: 5 s). Oliver and Pharr's method was used to find the contact penetration from the unloading curves.

The corrosion resistance of all the prepared coatings was investigated using a Gamry 3000 potentiostat/galvanostat/ZRA (Warminster, PA, USA). Saturated Ag/AgCl was used as reference, whereas graphite was used as counter, and coated samples were employed as working electrodes. After one hour at open circuit potential for stabilization, EIS experiments were carried out imposing an rms signal of 10 mV within the 10^5–10^{-2} Hz frequency range. Furthermore, the d.c. potentiodynamic polarization experiments were carried out at room temperature at a scan rate of 0.167 mVs^{-1} for a range of ±250 mV from open circuit potential prior to applying Tafel fit to determine the corrosion current and the corrosion potential [8,10,26].

3. Results and discussion

3.1. XRD measurements

X-ray diffraction spectra of Ni—P, Ni—P—0.5B₄C and Ni—P—1.0B₄C nanocomposite coatings are presented in Fig. 2 to study their structural characteristics. The wider peaks in
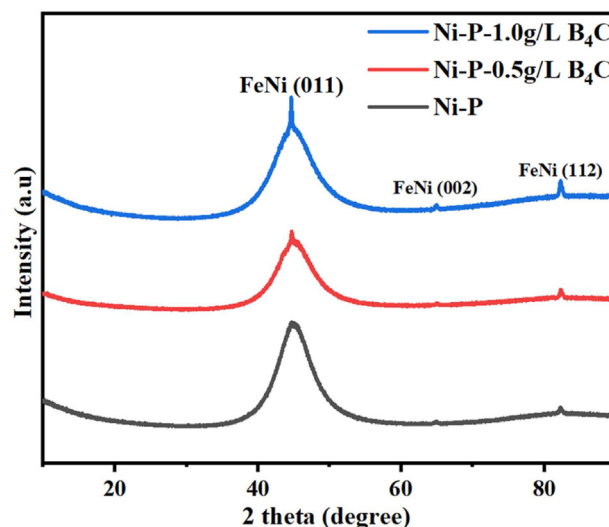

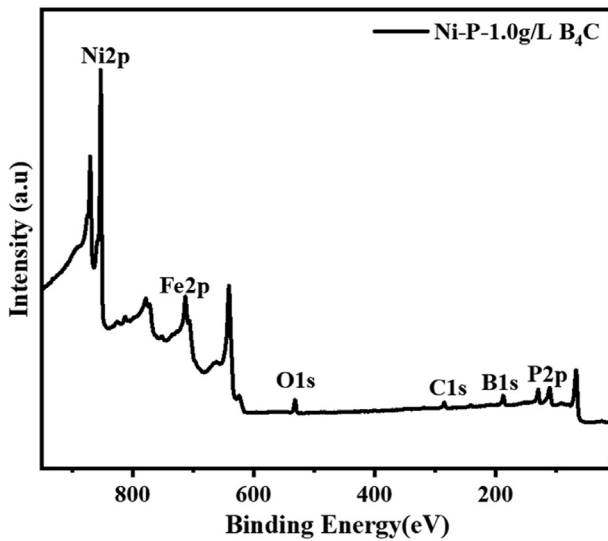**Fig. 2 — XRD spectra of Ni—P, Ni—P—0.5 g/L B₄C and Ni—P—1.0 g/L B₄C.**

Fig. 3 − XPS survey spectra of the Ni−P−1.0 g/L B$_4$C nanocomposite coating.

the spectra of all the coatings indicates the amorphous like structure that has been reported for higher phosphorus content (more than 8%) in the literature. Electrolytic formation of nickel and iron takes places in the FCC structure with phosphorus being codeposited at octahedral interstitial sites. The higher P content promotes the formation of an amorphous structure owing to the disturbance caused in the regular arrangement of Fe and Ni atoms [27]. The hump around $2\theta = 44°$ marks the formation of face-centered cubic lattice structure of Fe−Ni (011) plane, which has been distorted by the incorporation of phosphorus atoms resulting the formation of amorphous like structure [28,29]. Moreover, introducing BCNPs in the chemical bath led to a slight change and the amorphous structure evolves to a less amorphous one; the peak observed at $2\theta = 44.7°$ indicates the formation of Fe−Ni as per the file number 98-063-2932. Furthermore, increasing the concentration of BCNPs has increased the intensity of sharper peak s at $2\theta = 44.7$ suggesting further improvement in the crystallinity. This crystalline structure could be attributed to the heterogeneous nucleation caused by the BCNPs to the progressive development of the crystallite and diffusion of
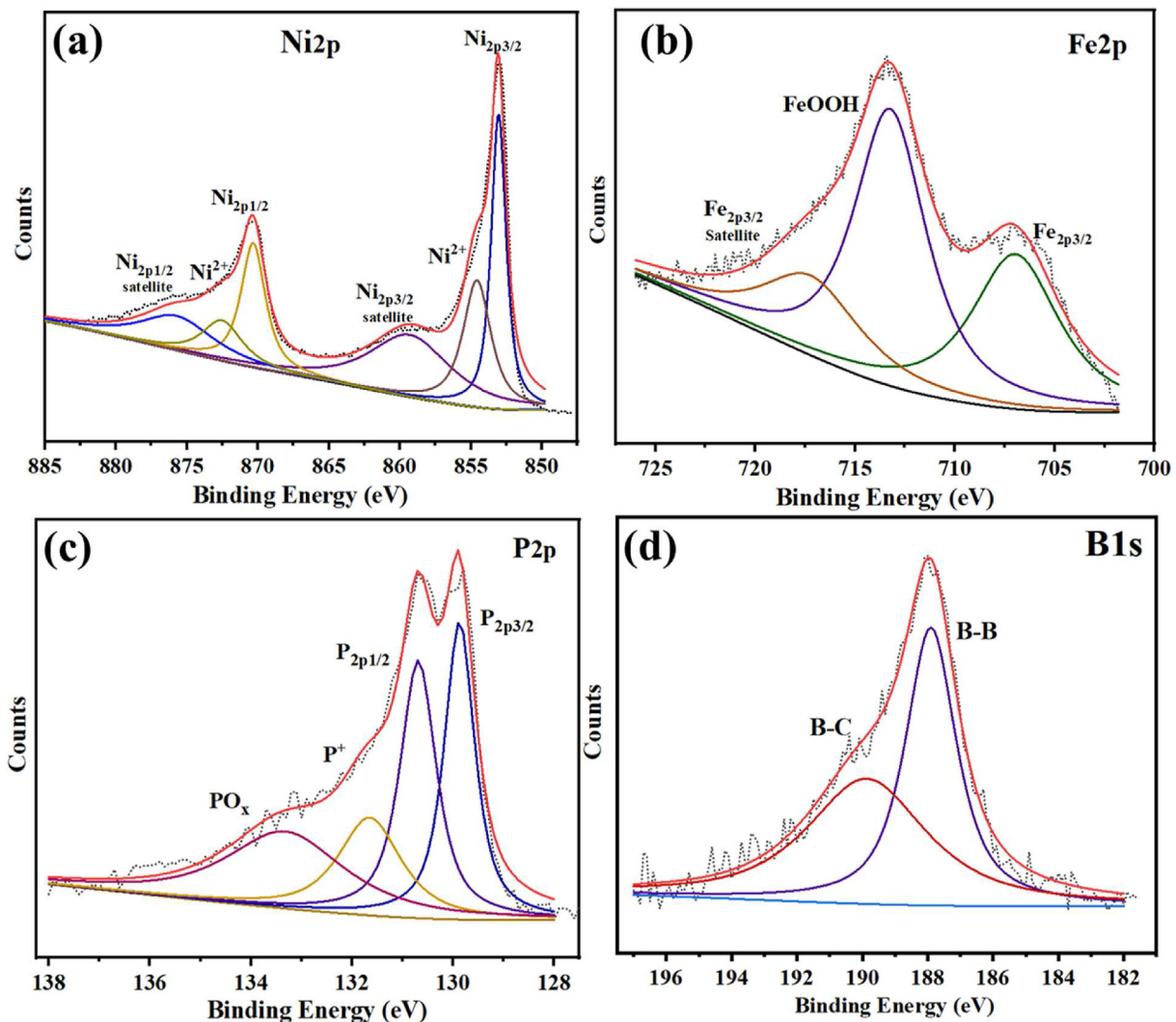

Fig. 4 − XPS spectra of Ni−P−1.0 g/L B$_4$C (a) Ni2p, (b) Fe2p, (c) P2p and (d) B1s.
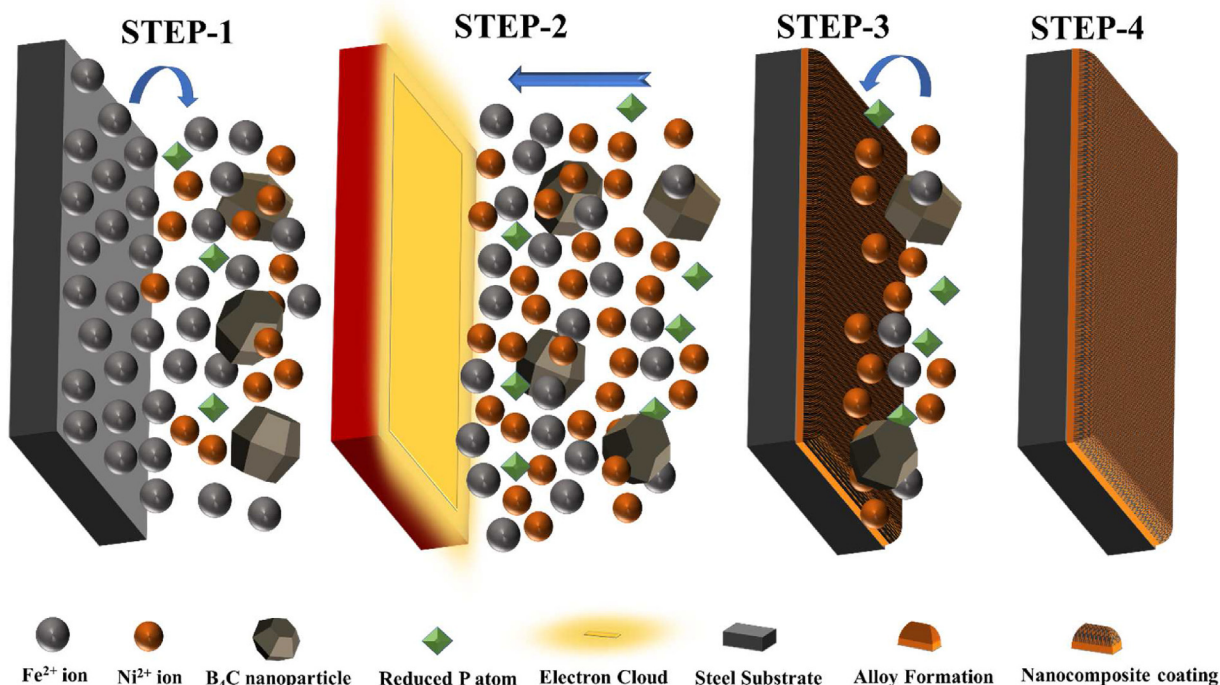
Fig. 5 — Schematic of the proposed deposition mechanism of Ni—P—B$_4$C nanocomposite coating.

nickel during deposition [8,30]. Peaks of BCNPs are not visible in reinforced nanocomposite coatings which can be associated to the very low percentage of BNCPs in the deposit and/or the shielding effect created by the broad peak of Fe—Ni as suggested by similar previous studies [31,32].

3.2. XPS analysis

Fig. 3 represents the XPS survey spectra of Ni—P—1.0 g/L B$_4$C nanocomposite coating. The presence of main elemental peaks corresponding to Ni$_{2p}$, Fe$_{2p}$, O$_{1s}$, C$_{1s}$, B$_{1s}$, and P$_{2p}$ are clearly visible. Peak representing oxygen could be due to the formation of superficial oxides or impurities prior to the installation of sample for analysis.

High magnification photoionizations of the respective elements are presented in Fig. 4. The experimental data was smoothened and Lorentzian—gaussian fit was utilized with background correction carried through Tougaard method for deconvoluting the respective chemical states of the elements. High energy resolution (HER) spectra in Fig. 4(a) lies within the range of 850 eV—885 eV binding energy represents the Ni2p photoionization. Deconvoluted peaks at 852.5 eV represents Ni$_{2p3/2}$ and 870.5 eV represents Ni$_{2p1/2}$ can be assigned to metallic Ni with their satellites peaks on 859.5 eV and 876.5 eV. Moreover, the peak identified at whereas the rest of the peaks located at 855.1 eV and 872.4 can be ascribed to the oxides and/ or hydroxides of nickel for the Ni^{2+} chemical state [8,10,32]. Fig. 4(b) displays the HER spectra of Fe$_{2p3/2}$, the peak around 707 eV can be attributed to metallic iron and the peak at 716.7 eV can be ascribed to its satellite, whereas the peaks located at 713.1 eV can be attributed to the formation iron oxyhydroxide. These compositions might have arisen as a

result of the dissolution of iron into the chemical bath due to high temperature and higher acidic conditions of the deposition before the power supply is connected to the anode and cathode [33—36] or contact with air moisture during sample handling. Fig. 4(c) shows the deconvoluted peaks of phosphorus (P2p), the peaks positioned at 129.8 eV and 130.7 eV can be ascribed to phosphorus of P2$_{p3/2,}$ and P2$_{p1/2.}$ However, the peak at 135.9 eV can be assigned to either intermediate chemical states of phosphorus or hypophosphite that remains as the solid solution in nanocomposite coatings. Moreover, the broad peak at 135.9 eV can be assigned to the oxides or hydroxides of phosphorus in their respective chemical state [8,10,32,37]. Fig. 4(d) depicts deconvoluted peaks of B1s, confirming the presence of boron carbide phase with peaks at 187.9 eV and 189.5 eV for B—B and B—C bonds [38,39]. The absence of any other oxidation state of B1s can be accepted as the inactive and inert nature of reinforcement toward the reactions occurring in the chemical bath during the entire electrodeposition process.

Co-deposition mechanism have been explained by various researchers for the formation of composite coatings, the summarized version of which is available in our previous articles [26]. In this study, we propose that initially iron dissolution from the substrate into the chemical bath takes place due to high temperature and lower pH of the chemical bath supporting the corrosion of the activated mild steel substrate. When the power supply is switched on, the electron cloud at the cathode surface initiates the reduction of ions from the chemical bath. This leads to the convective movement of the particles towards the cathode up to hydrodynamic layer of the cathode surface from bulk electrolyte. Moreover, in the hydrodynamic layer, a combination of electrophoresis and van
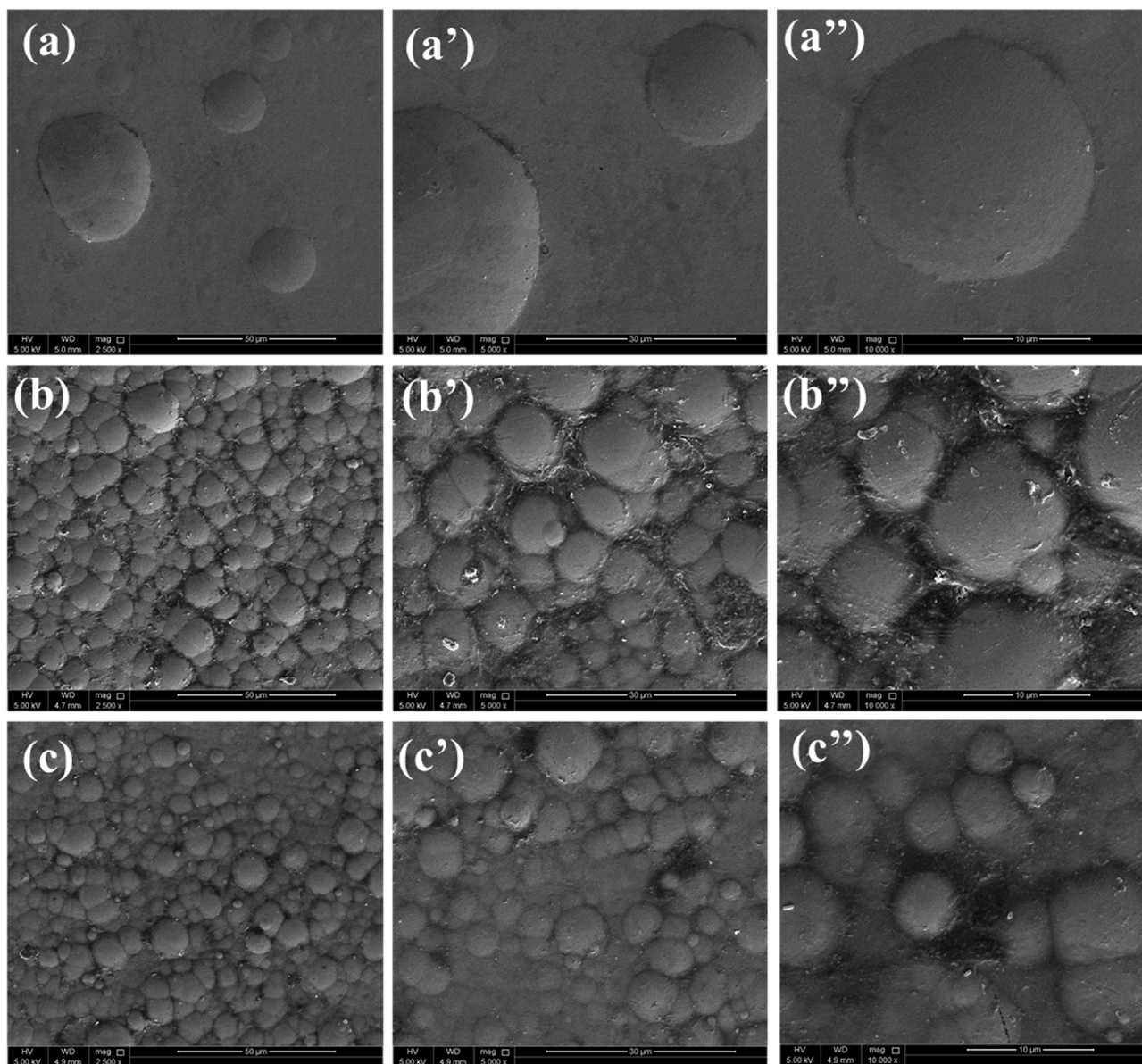
Fig. 6 — SEM micrograph of Ni—P at (a) 2500×, (a') 5000×, (a") 10000×, Ni—P—0.5 g/L B₄C (b) 2500×, (b') 5000×, (b") 10000× and Ni—P—1.0 g/L B₄C (c) 2500×, (c') 5000×, (c") 10000×.

der Waals effect seem to be more effective in forcing the reinforcement onto the cathode surface where it gets permanently entrapped owing to the reduction of ionic species around the reinforcement leading to the formation of nanocomposite structure [40–43]. This process is schematically shown in Fig. 5.

3.3. Surface morphology

AFM and FESEM were used to study the morphological and topographical characteristics of the as-prepared nanocomposite coatings. FE-SEM micrographs of Ni—P and Ni—P-BCNPs nanocomposite coatings are depicted in Fig. 6. As observed in the micrograph, Ni—P coatings Fig. 6 (a, a' and a") have sparsely irregular nodular structure without any regular granular geometry supporting the amorphous nature of pure

Ni—P coating [44]. Introducing BCNPs in the chemical bath has completely changed the morphology to irregular globular structure suggesting the restriction of the formation of large nodular structure of pure Ni—P as seen for the Ni—P—0.5 g/L B₄C in Fig. 6 (b, b' and b") [45,46].

Moreover, when the concentration of BCNPs increased in the chemical bath for Ni—P—1.0 g/LB₄C, further grain refinement is observed as the size of irregular globular grains has decreased, which is evident at various magnifications in Fig. 6 (c, c' and c") [47–49]. These results are coherent with the XRD spectra as the structural properties of pure Ni—P coating changed from amorphous to semi-amorphous or weak crystalline by increasing the concentration of BCNPs in the chemical bath. Moreover, the surface of the coatings was observed to be crack-free indicating good quality of the developed Ni—P and Ni—P-BCNPs nanocomposite coatings. The
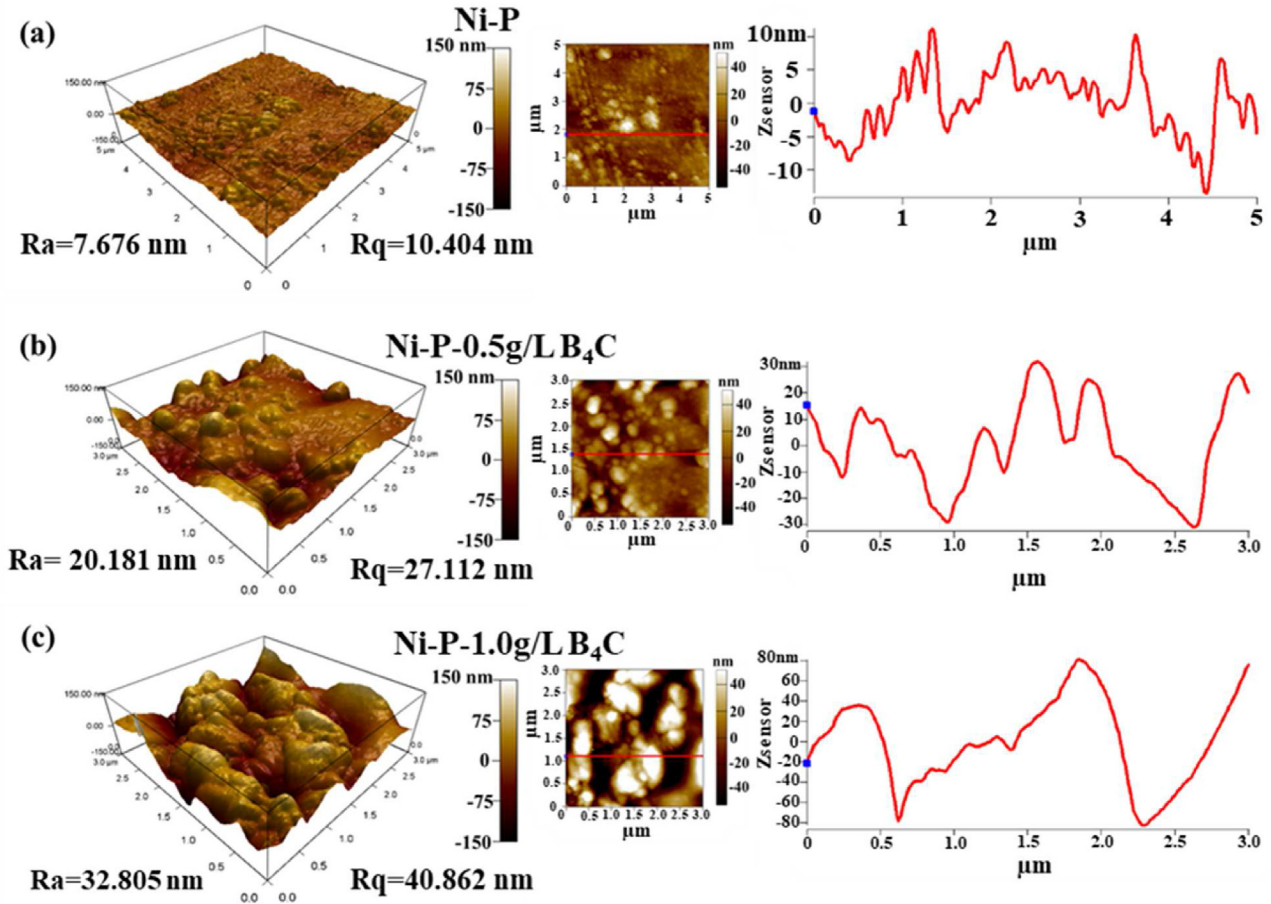
Fig. 7 — AFM profile of (a) Ni—P, (b) Ni—P—0.5 g/L B$_4$C and (c) Ni—P—1.0 g/L B$_4$C.

average thicknesses of all the coatings were around ~14.0 μm, achieved under the optimized experimental conditions.

The incorporation of BCNPs has enhanced the grain growth and increased the surface roughness of the coatings, which can be observed in the 3D AFM images, see Fig. 7 (a, b, c). The corresponding profiles of roughness for Ni—P and Ni—P-BCNPs nanocomposite coatings are also displayed for a clear comparison. The Ra (arithmetic mean roughness) of the Ni—P
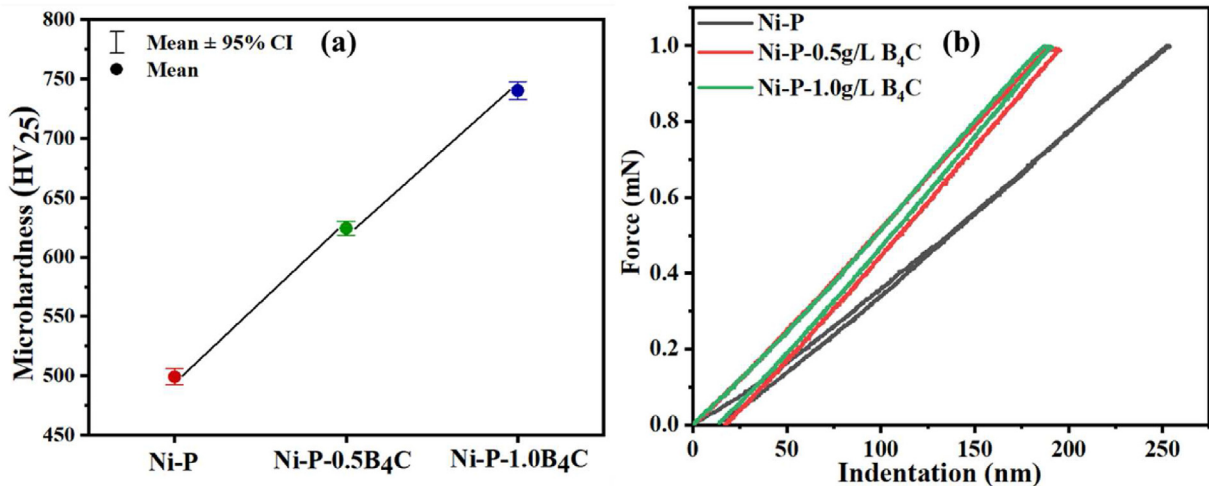

Fig. 8 — (a) Nanoindentation Profile (b) Vickers Microhardness results of Ni—P, Ni—P—0.5 g/L B$_4$C and Ni—P—1.0 g/L B$_4$C nanocomposite coating.

Table 2 — Nanoindentation results of Ni—P and Ni—P—BCNPs reinforced nanocomposite coatings.

Characteristic	Ni—P	Ni—P—0.5 g/LB$_4$C	Ni—P—1.0 g/LB$_4$C
Plasticity	−2.08	−1.54	−0.83
Elastic Modulus-E$_c$ (GPa)	8.68	13.26	14.44
Maximum Indentation-Depth H$_{max}$ (nm)	253.53	199.78	193.72
Final Indentation Depth H$_c$ (nm)	90.43	82.07	72.86
Hardness (GPa)	5.00	6.07	7.65

coating is ~ 7.7 nm, which rises to 20.1 nm on the addition of 0.5 g/L of BCNPs into the matrix; as the concentration of BCNPs is increased to 1.0 g/L, Ra further increases to a value of 32.8 nm; this growth in the surface roughness can be associated to the successful incorporation of inert, insoluble and extremely hard BCNPs in the matrix. Furthermore, R$_q$ (root mean square roughness) of Ni—P coatings increases from 10.4 nm to 27.1 nm and further to 40.8 nm for the increased concentration of BCNPs showing the consistency in the roughness trend.

Topographical comparison of surface roughness is displayed in Fig. 7 for Ni—P, Ni—P—0.5 g/L B$_4$C and Ni—P—1.0 g/L B$_4$C nanocomposite coatings. Hard and inert BCNPs resulted into the increased roughness of the pure Ni—P coating. Fig. 7 also provides the roughness profile revealing the consistency of the results [50,51].

3.4. Mechanical properties

The mechanical properties of Ni—P coating and BCNPs reinforced nanocomposite coating were investigated through Vickers microhardness and nanoindentation techniques. Fig. 8(a) displays the microhardness results revealing an incremental trend with the introduction and increasing of BCNPs in the chemical bath. In case of pure Ni—P coatings, the average microhardness is around 498 ± 12 HV$_{25}$, which increases to 623 ± 8 HV$_{25}$ as a result of introducing 0.5 g/L of BCNPs in the chemical bath that is 25.1% in comparison to pure Ni—P coatings. Microhardness furthers increases to 742 ± 15 HV$_{25}$ for the increased concentration of BCNPs to 1.0 g/L resulting in total increase of 48.9% from the pure Ni—P coating. The incremental trend of hardness can be ascribed to the successful formation of the composite structure where BCNPs are behaving as reinforcement and Fe—Ni—P solid solution acts as matrix giving rise to the dispersion hardening effect [10,52]. Moreover, nanoindentation technique was utilized to further analyze the mechanical properties at nano scale. Fig. 8 (b) shows the loading and unloading profile of Ni—P and BCNPs reinforced nanocomposite coatings and various properties were determined by Oliver and Pharr method and listed in Table 2 to elucidate its properties.

The maximum indentation depth of pure Ni—P coating decreased from 253.5 nm to 199.8 nm when 0.5 g/L of BCNPs were introduced in the chemical bath. A further decrease to 193.7 nm was observed for 1.0 g/L BCNPs marking the resistance offered by nanocomposite coating to the indenter for 1.0 mN of force. Similarly, elastic modulus (Ec) also increased from 8.68 GPa to a maximum value of 14.44 GPa along with the hardness, which increased from 5.0 GPa to 7.6 GPa for the incorporation of 1.0 g/L of BCNPs. The increase in elastic modulus and hardness can be attributed to the combination of dispersion hardening, grain refinement and formation of composite structure [30,53,54]. It can be ascribed as the incorporated hard BCNPs restrict the slip dislocation resulting in improved fracture mechanics. Moreover, continuous and smooth indentation profile also indicates the minimized surface defect of the coatings. It is worthy to note the decrease in the plasticity of nanocomposite coatings as a result of incorporating BCNPs, attributed to restriction offered by hard nanoparticles to the flow of solid solution matrix.
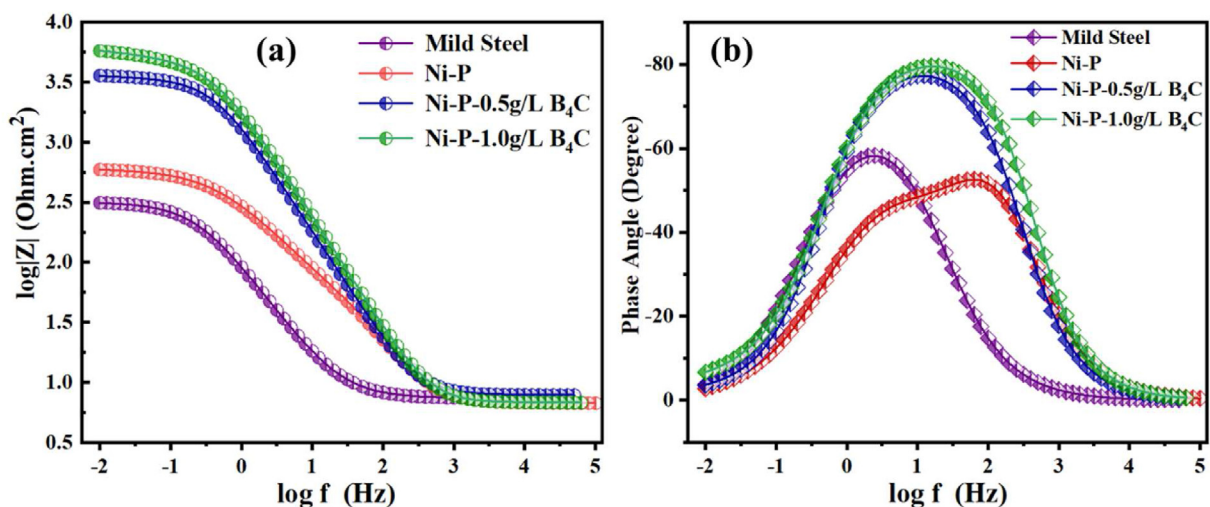

Fig. 9 — (a) Bode plots of the mild steel substrate, Ni—P, Ni—P—0.5 g/L-B$_4$C and Ni—P—1.0 g/L-B$_4$C nanocomposite coatings containing frequency impedance magnitude curve and (b) frequency phase angle curve after one hour of immersion in 3.5 wt.% NaCl solution.
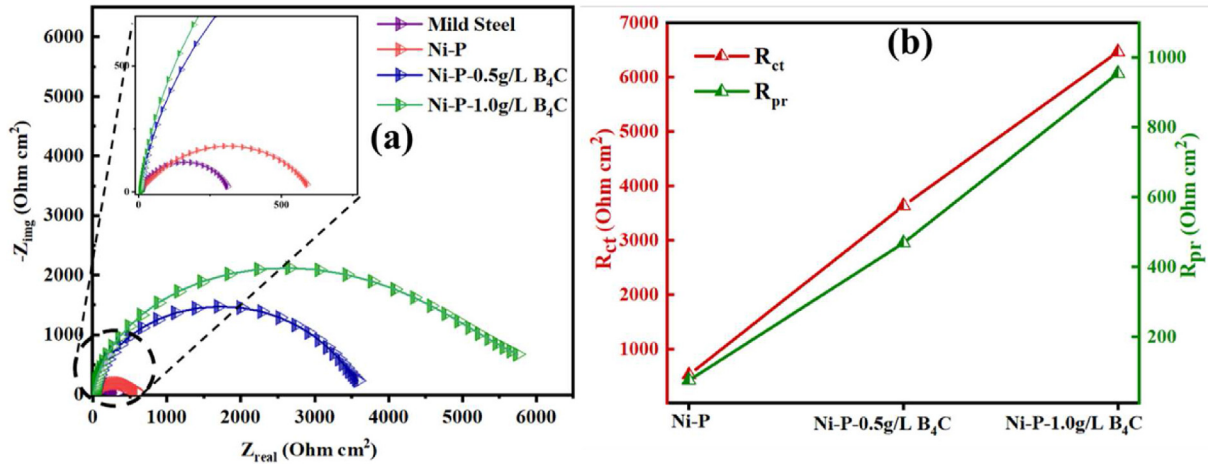
Fig. 10 − a) Nyquist plot for mild steel substrate and the as-fabricated Ni−P, Ni−P−0.5 g/L B₄C and Ni−P−1.0 g/L B₄C nanocomposite coatings in 3.5 wt% NaCl solution (b) difference of Rpr and Rct on the Ni−P, Ni−P−0.5 g/L B₄C and Ni−P−1.0 g/L B₄C nanocomposite coatings.
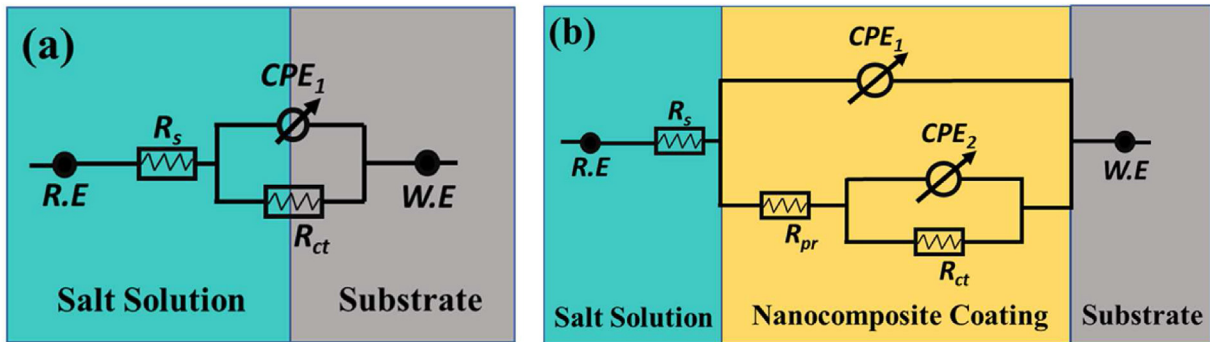

Fig. 11 − Equivalent electric circuit applied to fit EIS data for (a) mild steel substrate, (b) Ni−P, Ni−P−0.5 g/L B₄C and Ni−P−0.5 g/L B₄C nanocomposite coatings.

3.5. Corrosion studies

3.5.1. Electrochemical studies

EIS graphs of mild steel substrate, Ni−P, Ni−P−0.5 g/L B₄C and Ni−P−1.0 g/L B₄C nanocomposite coatings are shown in Fig. 9. Fitting of the mild steel substrate was carried out using the equivalent circuit shown in Fig. 10 (a). The capacitive element was replaced by a constant phase element to account for non-homogeneity of the electrode. To further understand the corrosion resistance mechanism of Ni−P and Ni−P−B₄C nanocomposite coating, a cascaded of two-time constants was used to model the EIS data, as described in Fig. 10(b). Elements described are R_s accounting for the electrolyte resistance (3.5wt% NaCl solution) used for the tests, R_{pr} and R_{ct} account for the resistive response of the pores and faradaic resistance between the interface bare metal-coating, respectively (see Fig. 11).

The constant phase element (CPE₁ and CPE₂) are given by eq. (1) [10]:
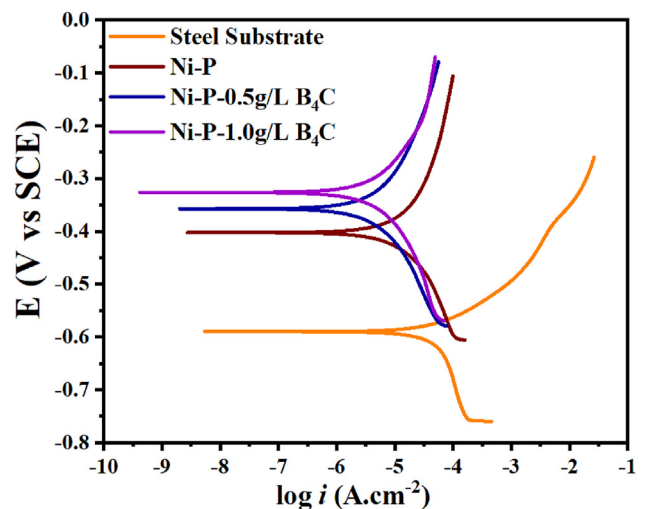
$$\frac{1}{Z_{CPE}} = Q(j\omega)^n \tag{1}$$

Fig. 12 − D.C. potentiodynamic plots of mild steel substrate, Ni−P coating, Ni−P−0.5 g/L B₄C and Ni−P−0.5 g/L B₄C nanocomposite coating.

Table 3 — Calculated Tafel parameters of mild steel substrate, Ni—P coating, Ni—P—0.5 g/L B₄C and Ni—P—0.5 g/L B₄C nanocomposite coating.

Sample	$\beta_{a(V/decade)}$	β_c (V/decade)	E_{corr} (mV)	I_{corr} ($\mu A/cm^2$)	PE% (Steel)	PE% (Ni—P)
Mild Steel	0.1734	0.9353	−591	400	—	—
Ni—P	0.8132	0.4486	−402	47	88.25%	—
Ni—P—0.5 g/L B₄C	0.3638	0.2957	−357	10.30	97.5%	76.6%
Ni—P—1.0 g/L B₄C	0.2748	0.2598	−326	9.31	97.7%	80.2%

in which Q stands for admittance, ω is the angular frequency, and n is the exponent for the constant phase element, which is responsible for the nature of capacitance such that closer to unity means pure capacitor.

The impedance results Fig. 9(a) reveal that the global impedance increases when the Ni—P coatings is modified with BCNPs in the Ni—P matrix.Impedance for mild steel substrate is around 310 Ω cm², which is half of the value determined for the Ni—P coating, with 601 Ω cm² total impedance. Improved corrosion resistance of the Ni—P coating can be described by the formation of corrosion resistant hypophosphite layer due to the electrochemical reaction of Ni—P coating as reported in the literature [55]. However, pure Ni—P coatings may contain defects and pores that still limit their corrosion resistance. However, the reinforcing particles may help to decrease these defects contributing to increase the overall coating impedance for the global impedance of the Ni—P—0.5 g/L B₄C was approximately 3363 Ω cm² that represents a 5 times increase of the corrosion resistance compared to the unmodified coating, in agreement with literature [8,30,52], along with the complex solid solution deposition product of the Ni, Fe, P and B₄C at the initial stage of the deposition explained earlier. Furthermore, increasing the concentration of B₄C still has a positive impact on the anti-corrosive behavior of the coating, as the corrosion resistance increased up to 6044 Ω cm². Moreover, BCNPs also resulted in broadening phase angle, including in the high frequency region, evidencing the increased protectiveness of nanocomposite coating as seen in Fig. 9(b).

The fitted Nyquist plots of mild steel substrate, Ni—P and BCNPs reinforced nanocomposite coating are displayed in Fig. 10(a). The inset in Fig. 10(a) is the enlarged to show the semicircular plots of mild steel substrate and pure Ni—P coating. The Higher corrosion resistance of nanocomposite coatings is well evidenced by the increasing Faradaic resistance in the presence of reinforcing particles. This result agrees well with previous ones already reported in the literature [8,30,52].

3.5.2. Tafel study

Potentiodynamic polarization studies were further carried out to assess the corrosion resistance of the BCNPs reinforced nanocomposite coatings. Tafel fit of the experimental data was carried out and the anodic slope (βa) and cathodic slope (βc), corrosion potential (E_{corr}), and corrosion current (I_{corr}) were obtained from the fitted curves (Fig. 12) and presented in Table 3. In addition, the efficiency of corrosion protection (PE %) was estimated with respect to mild steel substrate and pure Ni—P coating by using the formula stated in [8] as described in

Equation (2), where i_1 and i_2 are successive corrosion current of respective samples.

$$PE\% = 1 - \frac{i_2}{i_1} \qquad (2)$$

Mild steel substrate showed the more negative Ecorr −591 mV and icorr 400 μA/cm2 in comparison to pure Ni—P coating, which had −402 mV and 47 μA/cm2 values suggesting one order of magnitude increase in the corrosion resistance. Introducing and increasing the amount of BCNPs further increased the corrosion potential and decreased the corrosion current that reached values of 9.31 μA/cm² for Ni—P—1.0g/LB₄C nanocomposite coating. An overall improvement of 97.7% with respect to mild steel substrate and 80.2% in comparison to pure Ni—P coating was observed in the presence of 1.0 g/L of BCNPs. This can be ascribed to the successful incorporation of inert and hard boron carbide nano particles in the matrix of complex solid solution such that it reduces the active region and restricting the adsorption of chloride ions that initiate corrosion [56,57].

4. Conclusions

Ni—P—B₄C nanocomposite coatings were successfully produced in the presence of an increasing concentration of BCNPs. XRD studies revealed the coatings evolve from amorphous to weakly crystalline when the content of BCNPs increased. XPS results evidenced the chemical state of all the elements present in the developed coatings and a new expected deposition mechanism for the development of coating has been proposed. FE-SEM studies evidenced that the coating morphology changed from the sparsely globular structure of Ni—P to a more well-defined nodular structure demonstrating the refinement in the grain size with increasing the amount of BCNPs. Topographical images showed an increase in average roughness with the increase of BCNPs in the chemical bath. Vickers hardness was found to have improved from 500 to around 750 that is an increment of 40% as a result of reinforcing role of BCNPs in the Ni—P matrix. Nanoindentations further validated the microhardness results and computed elastic constant 14.44 GPa as a result of the incorporation of 1 g/L of BCNPs. Moreover, the electrochemical study confirmed an important increase of the corrosion resistance of Ni—P coatings after addition of BCNPs. The impedance values increased up to 6 kΩ cm² at 1.0 g/L, which was more than 5 times compared to that of pure Ni—P coatings and ~10 times in comparison to the bare mild steel substrate. This increased protection was confirmed by the Tafel analysis.

Overall, the results indicate that Ni—P—B$_4$C nanocomposite coatings have a high potential for replacement of counterparts for enhanced mechanical strength and corrosion protection in the presence of NaCl aggressive species.

Declaration of Competing Interest

The authors declare that they have no known competing financial interests or personal relationships that could have appeared to influence the work reported in this paper.

Acknowledgment

R E F E R E N C E S

[1] Amaya-Gómez R, Sánchez-Silva M, Bastidas-Arteaga E, Schoefs F, Muñoz F. Reliability assessments of corroded pipelines based on internal pressure — a review. Eng Fail Anal 2019;98:190—214.

[2] Zamani SM, Hassanzadeh-Tabrizi SA, Sharifi H. Failure analysis of drill pipe: a review. Eng Fail Anal 2016;59:605—23.

[3] Xie M, Tian Z. A review on pipeline integrity management utilizing in-line inspection data. Eng Fail Anal 2018;92:222—39.

[4] Shekari E, Khan F, Ahmed S. Economic risk analysis of pitting corrosion in process facilities. Int J Pres Ves Pip 2017;51—62.

[5] Lelevic A, Walsh FC. Electrodeposition of Ni P alloy coatings: a review. Surf Coating Technol 2019;369:198—220.

[6] Loto CA. Electroless nickel plating — a review. Silicon 2016;8(2):177—86.

[7] Chen B, Guo J, Yan MF, Wang F, Liu F. Study on a Ni-P-nano TiN composite coating for significantly improving the service life of copper alloy synchronizer rings. Appl Surf Sci 2020;504:144116.

[8] Bahgat Radwan A, Ali K, Shakoor RA, Mohammed H, Alsalama T, Kahraman R, et al. Properties enhancement of Ni-P electrodeposited coatings by the incorporation of nanoscale Y2O3 particles. Appl Surf Sci 2018;457:956—67.

[9] Li B, Zhang W, Huan Y, Dong J. Synthesis and characterization of Ni-B/Al2O3 nanocomposite coating by electrodeposition using trimethylamine borane as boron precursor. Surf Coating Technol 2018;337:186—97.

[10] Sliem MH, Shahzad K, Sivaprasad VN, Shakoor RA, Abdullah AM, Fayyaz O, et al. Enhanced mechanical and corrosion protection properties of pulse electrodeposited NiP-ZrO2 nanocomposite coatings. Surf Coating Technol 2020;403:126340.

[11] Wasekar NP, Bathini L, Ramakrishna L, Rao DS, Padmanabham G. Pulsed electrodeposition, mechanical properties and wear mechanism in Ni-W/SiC nanocomposite coatings used for automotive applications. Appl Surf Sci 2020;527:146896.

[12] Dhakal DR, Kshetri YK, Gyawali G, Kim T-H, Choi J-H, Lee SW. Understanding the effect of Si3N4 nanoparticles on wear resistance behavior of electroless Nickel-Phosphorus coating through structural investigation. Appl Surf Sci 2021;541:148403.

[13] Li B, Zhang W. A novel Ni-B/YSZ nanocomposite coating prepared by a simple one-step electrodeposition at different duty cycles. J Mater Res Technol 2020;9(2):1519—29.

[14] Li B, Mei T, Li D, Du S. Ultrasonic-assisted electrodeposition of Ni-Cu/TiN composite coating from sulphate-citrate bath: structural and electrochemical properties. Ultrason Sonochem 2019;58:104680.

[15] Giurlani W, Zangari G, Gambinossi F, Passaponti M, Salvietti E, Di Benedetto F, et al. Electroplating for decorative applications: recent trends in research and development. Coatings 2018;8(8).

[16] Zhao Y, Yu T, Chen L, Chen Y, Guan C, Sun J. Microstructure and wear resistance behavior of Ti—C—B4C-reinforced composite coating. 16, Part A Ceram Int 2020;46:25136—48.

[17] Pushpanathan DP, Alagumurthi N, Devaneyan SP. On the microstructure and tribological properties of pulse electrodeposited Ni-B4C-TiC nano composite coating on AZ80 magnesium alloy. Surf Interface 2020;19:100465.

[18] Xu Z, Xie Y, Ebrahimnia M, Dang H. Effect of B4C nanoparticles on microstructure and properties of laser cladded IN625 coating. Surf Coating Technol 2021;416:127154.

[19] Jiang JB, Zhang L, Zhong QD, Zhou QY, Wang Y, Luo J. Preparation and characterisation of nickel—nano-B4C composite coatings. Surf Eng 2012;28(8):612—9.

[20] Rezagholizadeh M, Ghaderi M, Heidary A, Monirvaghefi SM. The effect of B4C nanoparticles on the corrosion and tribological behavior of electroless Ni-B-B4C composite coatings. Surf Eng Appl Electrochem 2015;51(1):18—24.

[21] Ebrahimian-Hosseinabadi M, Azari-Dorcheh K, Moonir Vaghefi SM. Wear behavior of electroless Ni—P—B4C composite coatings. Wear 2006;260(1):123—7.

[22] Araghi A, Paydar MH. Electroless deposition of Ni—P—B4C composite coating on AZ91D magnesium alloy and investigation on its wear and corrosion resistance. Mater Des 2010;31(6):3095—9.

[23] Monir Vaghefi SM, Saatchi A, Ebrahimian-Hoseinabadi M. Deposition and properties of electroless Ni—P—B4C composite coatings. Surf Coating Technol 2003;168(2):259—62.

[24] He T, He Y, Li H, Su Z, Fan Y, He Z. Fabrication of Ni-W-B4C composite coatings and evaluation of its micro-hardness and corrosion resistance properties. Ceram Int 2018;44(8):9188—93.

[25] Bozzini B, Cavallotti PL, Parisi G. Corrosion and erosion-corrosion of electrodeposited Ni—P/B4 C composites. Br Corrosion J 2001;36(1):49—55.

[26] Fayyaz O, Bahgat Radwan A, Sliem MH, Abdullah AM, Hasan A, Shakoor RA. Investigating the properties of electrodeposited of Ni-P-ZrC nanocomposite coatings. ACS Omega 2021;6(49):33310—24.

[27] Alleg S, Boussaha A, Tebib W, Zergoug M, Suñol JJ. Microstructure and magnetic properties of NiP alloys. J Supercond Nov Magnetism 2016;29(4):1001—11.

[28] Yang Y, Chen W, Zhou C, Xu H, Gao W. Fabrication and characterization of electroless Ni—P—ZrO2 nano-composite coatings. Appl Nanosci 2011;1(1):19—26.

[29] Nava D, Dávalos C, Martínez-Hernández A, Federico M, Meas Y, Ortega R, et al. Effects of heat treatment on the

tribological and corrosion properties of electrodeposited Ni-P alloys. Int J Electrochem Sci 2013;8:2670—81.

[30] Shahzad K, Radwan AB, Fayyaz O, Shakoor RA, Uzma M, Umer MA, et al. Effect of concentration of TiC on the properties of pulse electrodeposited Ni—P—TiC nanocomposite coatings. Ceram Int 2021;47(13):19123—33.

[31] Safavi MS, Rasooli A. Ni-P-TiO2 nanocomposite coatings with uniformly dispersed Ni3Ti intermetallics: effects of current density and post heat treatment. Surf Coating Technol 2019;372:252—9.

[32] Luo H, Wang X, Gao S, Dong C, Li X. Synthesis of a duplex Ni-P-YSZ/Ni-P nanocomposite coating and investigation of its performance. Surf Coating Technol 2017;311:70—9.

[33] Yuan M, Nan C, Yang Y, Sun G, Li H, Ma S. Uniform FexNiy nanospheres: cost-effective electrocatalysts for nonaqueous rechargeable Li—O2 batteries. ACS Omega 2017;2(8):4269—77.

[34] Luo H, Dong C, Xiao K, Li X. The passive behaviour of ferritic stainless steel containing alloyed tin in acidic media. RSC Adv 2016;6(12):9940—9.

[35] Guo LQ, Qin SX, Yang BJ, Liang D. Effect of hydrogen on semiconductive properties of passive film on ferrite and austenite phases in a duplex stainless steel. Sci Rep 2017;7(1):3317.

[36] Li B, Mei T, Du S, Zhang W. Synthesis of Ni—Fe and Ni—Fe/ZrO2 composite coating and evaluation of its structural and corrosion resistance. Mater Chem Phys 2020;243:122595.

[37] Song G-S, Sun S, Wang Z-C, Luo C-Z, Pan C-X. Synthesis and characterization of electroless Ni—P/Ni—Mo—P duplex coating with different thickness combinations. Acta Metall Sin 2017;30(10):1008—16.

[38] Sun Y, Meng Q, Qian M, Liu B, Gao K, Ma Y, et al. Enhancement of oxidation resistance via a self-healing boron carbide coating on diamond particles. Sci Rep 2016;6(1):20198.

[39] Mishra A, Sahoo RK, Singh SK, Mishra BK. Synthesis of low carbon boron carbide powder using a minimal time processing route: thermal plasma. J Asian Ceram Soc 2015;3(4):373—6.

[40] Berçot P, Peña-Muñoz E, Pagetti J. Electrolytic composite Ni—PTFE coatings: an adaptation of Guglielmi's model for the phenomena of incorporation. Surf Coating Technol 2002;157(2):282—9.

[41] Bahadormanesh B, Dolati A. The kinetics of Ni—Co/SiC composite coatings electrodeposition. J Alloys Compd 2010;504(2):514—8.

[42] Fransaer J, Celis JP, Roos JR. Analysis of the electrolytic codeposition of non-brownian particles with metals. J Electrochem Soc 1992;139(2):413—25.

[43] Celis JP, Roos JR, Buelens C. A mathematical model for the electrolytic codeposition of particles with a metallic matrix. J Electrochem Soc 1987;134(6):1402—8.

[44] Meshram AP, Punith Kumar MK, Srivastava C. Enhancement in the corrosion resistance behaviour of amorphous NiP

coatings by incorporation of graphene. Diam Relat Mater 2020;105:107795.

[45] Ankita S, Singh A. Corrosion and wear resistance study of Ni-P and Ni-P-PTFE nanocomposite coatings. J Open Eng 2011;1(3):234—43.

[46] Ahmadkhaniha D, Zanella C. The effects of additives, particles load and current density on codeposition of SiC particles in NiP nanocomposite coatings. Coatings 2019;9(9):554.

[47] Zhang W, Cao D, Qiao YX, He Z, Wang Y, Li X, et al. Microstructure and properties of duplex Ni-P-TiO2/Ni-P nanocomposite coatings. Mater Res 2019;22.

[48] Madhukar P, Mishra V, Selvaraj N, Rao CSP, Gonal Basavaraja VK, Seetharam R, et al. Influence of ultrasonic vibration towards the microstructure refinement and particulate distribution of AA7150-B4C nanocomposites. Coatings 2022;12(3):365.

[49] Bahrami F, Amini R, Taghvaei AH. Microstructure and corrosion behavior of electrodeposited Ni-based nanocomposite coatings reinforced with Ni60Cr10Ta10P16B4 metallic glass particles. J Alloys Compd 2017;714:530—6.

[50] Fayyad EM, Abdullah AM, Hassan MK, Mohamed AM, Wang C, Jarjoura G, et al. Synthesis, characterization, and application of novel Ni-P-carbon nitride nanocomposites. Coatings 2018;8(1):37.

[51] Shahzad K, Fayyad EM, Nawaz M, Fayyaz O, Shakoor RA, Hassan MK, et al. Corrosion and Heat Treatment Study of Electroless NiP-Ti Nanocomposite Coatings Deposited on HSLA Steel. Nanomaterials 2020;10(10):1932.

[52] Radwan AB, Shakoor RA. Aluminum nitride (AlN) reinforced electrodeposited Ni—B nanocomposite coatings. Ceram Int 2020;46(7):9863—71.

[53] Li H, He Y, Luo P, Fan Y, Yu H, Wang Y, et al. Influence of pulse frequency on corrosion resistance and mechanical properties of Ni-W/B4C composite coatings. Colloids Surf A Physicochem Eng Asp 2021;629:127436.

[54] Sajjadnejad M, Haghshenas SMS, Tavakoli Targhi V, Setoudeh N, Hadipour A, Moghanian A, et al. Wear behavior of alkaline pulsed electrodeposited nickel composite coatings reinforced by ZnO nanoparticles. Wear 2021;468—469:203591.

[55] Luo H, Leitch M, Zeng H, Luo J-L. Characterization of microstructure and properties of electroless duplex Ni-W-P/Ni-P nano-ZrO2 composite coating. Mater Today Phys 2018;4:36—42.

[56] Sadreddini S, Salehi Z, Rassaie H. Characterization of Ni—P—SiO2 nano-composite coating on magnesium. Appl Surf Sci 2015;324:393—8.

[57] Farzaneh A, Mohammadi M, Ehteshamzadeh M, Mohammadi F. Electrochemical and structural properties of electroless Ni-P-SiC nanocomposite coatings. Applied Surface Science 2013;276:697—704.